Optically Induced Tunable Magnetization Dynamics in Nanoscale Co Antidot Lattices

Ruma Mandal,[†] Susmita Saha,[†] Dheeraj Kumar,[†] Saswati Barman,[†] Semanti Pal,[†] Kaustuv Das,[†] Arup Kumar Raychaudhuri,[†] Yasuhiro Fukuma,[‡,§] YoshiChika Otani,[‡,⊥] and Anjan Barman[†,*]

[†]Department of Condensed Matter Physics and Material Sciences, S. N. Bose National Centre for Basic Sciences, Block JD, Sector III, Salt Lake, Kolkata 700 098, India, [‡]Advanced Science Institute, RIKEN, 2-1 Hirosawa, Wako, Saitama 351-0198, Japan, [§]Frontier Research Academy for Young Researchers, Kyushu Institute of Technology, Iizuka, Fukuoka, 820-8502, Japan, and [⊥]Institute for Solid State Physics, University of Tokyo, 5-1-5 Kashiwanoha, Kashiwa, Chiba 277-8581, Japan

Nanoscale ferromagnetic antidot (hole) lattices have emerged as a system of intense interest as magneto-photonic crystals due to the influence of the magnetic field on the light coupling to surface plasmons.[1−3] Magnetic antidots have also been considered as a candidate for ultrahigh density data storage devices,[4] so that the memory bit could be trapped between consecutive holes along the intrinsic hard axis of the antidot nanostructure.[5] The antidots have some advantages at the deep nanoscale dimensions due to the absence of any isolated small magnetic entity, and they do not suffer from the superparamagnetic bottleneck. However, one of their most exciting prospects is in the magnonic crystals,[6−8] where the magnonic band structures can be manipulated by the periodic arrays of magnetic antidots. Magnonic crystals are spatially modulated magnetic mediums, analogous to photonic or phononic crystals in the microwave band, which may open up magnonic band gaps for the propagating magnons, leading toward applications in on-chip nanoscale microwave communications. The periodic modulation is limited not only at the physical boundaries of the antidots but also at the strong pinning centers for spin waves created by the demagnetized regions between the antidots. Magnetic antidot lattices are exchange-coupled magnetic systems as opposed to the magnetostatically coupled magnetic dot lattices and hence offer much higher propagation velocity (steeper frequency *vs* wavevector dispersion) and longer propagation length for the magnons than the dot lattices before the excitation is decayed. More recently, filled antidots have raised interests as bicomponent magnonic crystals,[9,10] where the differences between the magnetic parameters of two magnetic

ABSTRACT
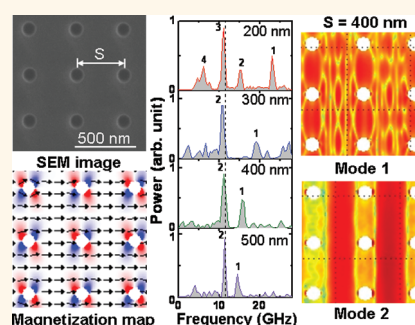
We report the time-domain measurements of optically induced precessional dynamics in a series of Co antidot lattices with fixed antidot diameter of 100 nm and with varying lattice constants (*S*) between 200 and 500 nm. For the sparsest lattice, we observe two bands of precessional modes with a band gap, which increases substantially with the decrease in *S* down to 300 nm. At *S* = 200 nm, four distinct bands with significant band gaps appear. The numerically calculated mode profiles show various localized and extended modes with the propagation direction perpendicular to the bias magnetic field. We numerically demonstrate some composite antidot structures with very rich magnonic spectra spreading between 3 and 27 GHz based upon the above experimental observation.

KEYWORDS: magnetic nanostructures · time-resolved magneto-optical Kerr effect · magnetization precession · magnonic crystals · band gap

mediums provide additional tunability in the magnonic band structures.

One of the important issues regarding the various applications of magnetic antidot lattices is the successful fabrication of good quality structures with smaller dimensions and the time-domain detection of the magnetization dynamics in such materials. So far, the reported experimental results have been primarily confined to antidots with micrometer to several hundreds of nanometers of dimensions.[5,11−22] The lithographic techniques including e-beam lithography and focused ion beam lithography often
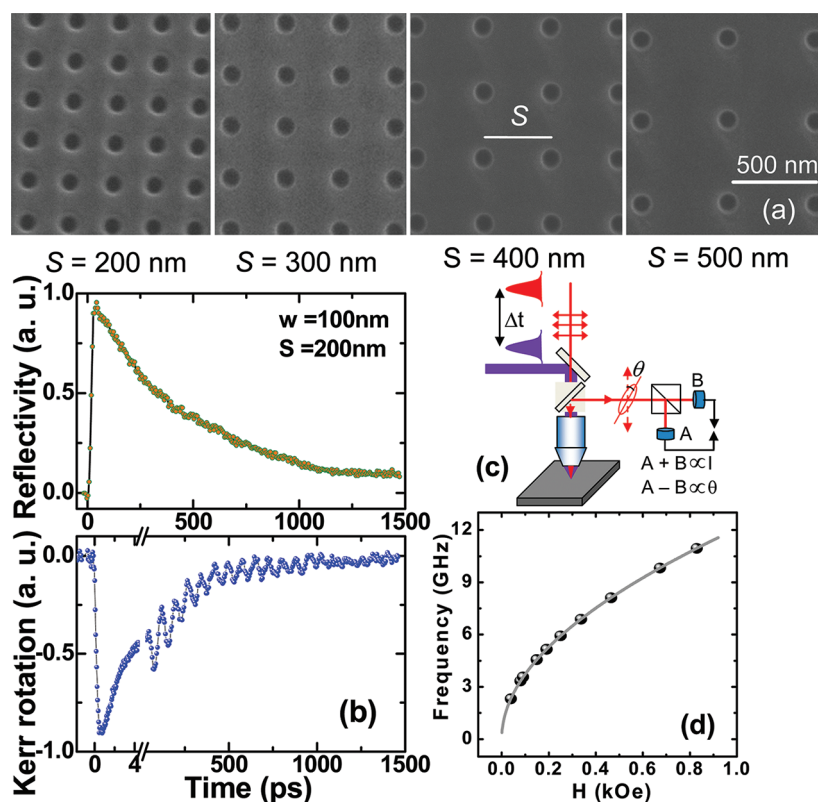
Figure 1. (a) Scanning electron micrographs of the antidot lattices with width $w = 100$ nm and with variable lattice constant S. (b) Time-resolved reflectivity and Kerr rotation for the antidot lattice with $S = 200$ nm at a bias field $H = 0.9$ kOe. (c) Schematic of the time-resolved Kerr microscope. (d) Experimental precession frequencies (symbols) as a function of the bias magnetic field for a $10 \times 10 \ \mu m^2$ Co film with 25 nm thickness and the fit to the Kittel's formula (solid curve).

create defects at the edges of the antidots at the deep nanometer scale, providing additional pinning regions, which may significantly modify the magnonic spectra of the intrinsic lattice. On the other hand, the measurements of magnetization dynamics of magnetic antidot lattices have been primarily done by Brillouin light scattering[14−17,19,21] and broad-band ferromagnetic resonance measurements,[11,16−18,20,23] while there is only a single report on the time-domain observation of precessional dynamics from microscale CoFeB antidot lattices.[24] In the early works, attenuation of uniform ferromagnetic resonance mode due to the excitation of non-uniform in-plane spin wave mode[20] and pattern-induced frequency splitting of propagating spin waves[19] were observed. More recently, field-controlled and anisotropic propagation[17,25] of spin waves, spin wave localization,[18,25] and magnonic miniband formation with large spin wave velocities[16] have attracted attention. Further experiments such as spatial control of spin wave modes in bicomponent antidots[10] and angular variation of the dynamics by tailoring lattice symmetry[15,26] have been initiated. However, tunability of magnonic band gaps with the variation of physical parameters of the nanoscale antidot lattices and understanding the origin of such tunability have not been reported in the literature. Here, we report the fabrication of high-quality Co antidot lattices with 100 nm

antidot diameters and with lattice constant (S) varying between 200 and 500 nm. We have excited and detected the precessional dynamics in the antidot lattices by an all-optical method. We observe a significant variation in the dynamics with the variation in the lattice constant, including a tunable gap in the magnonic spectra from the experimental results and micromagnetic simulations. Finally, we propose composite antidot structures with very rich magnonic spectra based upon the above observation.

RESULTS AND DISCUSSION

Each antidot lattice was fabricated on square-shaped Co blanket films of 10 μm width and 25 nm thickness. This is to physically isolate the antidot lattices from each other so that there is no magneto-static or exchange interactions between the lattices, and the dynamics of any individual lattice is not affected by the presence of other lattices. The Co blanket thin films were prepared by electron beam evaporation on Si(100) substrates with a thin SiO$_2$ layer on top of the substrate, and UV optical lithography was used to pattern the film for edge-to-edge spacing of 10 μm. This was followed by milling of square arrays of antidots of circular shapes on each blanket Co film by using focused ion beam lithography. The circular holes were made with fixed 100 nm antidot diameters and
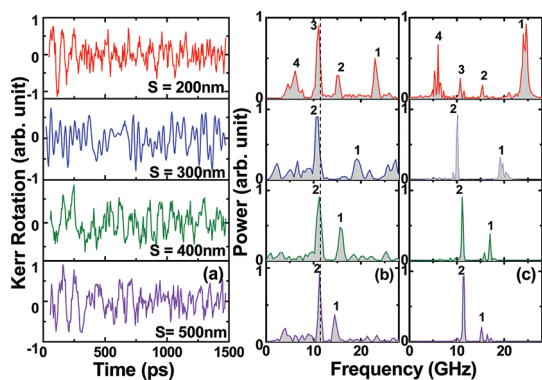
Figure 2. (a) Measured time-resolved Kerr rotations and (b) corresponding FFT spectra are shown for antidot lattices with variable lattice constants at $H = 0.9$ kOe. (c) FFT spectra of the simulated time-resolved magnetization. The mode numbers are assigned to the peaks of each band.

with variable lattice constants of 200, 300, 400, and 500 nm. Figure 1a presents the scanning electron micrographs of the lattices, which show that the samples are generally well fabricated with small deviations in the antidot diameters and lattice constants, which will eventually be included in the micromagnetic simulations to the extent possible under the finite difference method. One blanket Co film with 10 μm width and 25 nm thickness was used for measuring the magnetic parameters of the unpatterned sample. Static magneto-optical Kerr effect measurements of magnetic hysteresis loops with the magnetic field applied at varying azimuthal angle reveal that the samples have negligible magnetic anisotropy. This is possibly due to the highly polycrystalline nature of the thin films with randomly oriented grains grown by e-beam evaporation. The all-optical excitation and time-domain detection of the magnetization dynamics were done by a home-built two-color all-optical time-resolved magneto-optical Kerr microscope.[27] The bias field was tilted at a 15° angle from the plane of the sample (H = component of the bias field along the x-direction) to have a finite demagnetizing field along the direction of the pump pulse, which is eventually modified by the pump pulse to induce precessional magnetization dynamics within the samples.

Figure 1b shows that the precessional dynamics appears as an oscillatory signal above the slowly decaying part of the time-resolved Kerr rotation signal after a fast demagnetization within 500 fs, and a fast remagnetization with a time constant of 5.2 ps. The schematic of the measurement setup is shown in Figure 1c. A biexponential background is subtracted from the time-resolved Kerr signal before performing the fast Fourier transform (FFT) to find the corresponding power spectra. The reflectivity data, on the other hand, show a sharp increase at zero delay and a biexponential decay.

The magnetization dynamics of a 10 × 10 μm² square Co film was measured at varying bias field values by placing the pump and probe beams at the

center of the pattern. The FFT spectra show a single precession frequency, which is plotted as a function of the bias field in Figure 1d. The experimental data are fitted with the Kittel's formula for the uniform precession of magnetization as given in eq 1.

$$f = \frac{\gamma}{2\pi}\sqrt{(H + H_K)(H + H_K + 4\pi M_S)} \qquad (1)$$

The magnetic parameters extracted from the fit are gyromagnetic ratio $\gamma = 17.6$ MHz/Oe, magneto-crystalline anisotropy field $H_K \approx 0$, and the saturation magnetization $M_S = 1400$ emu/cc. These magnetic parameters will later be used in micromagnetic simulations of the Co antidot structures. Figure 2a shows the background-subtracted time-resolved Kerr rotation data and the corresponding FFT spectra (Figure 2b) from the Co antidot lattices with varying lattice constants from 200 to 500 nm at $H = 0.9$ kOe. In Figure 2b, we show the precession frequency of the unpatterned thin film as a vertical dotted line. Two clear bands of modes are observed for $S = 500$, 400, and 300 nm, and the band gap increases consistently and significantly with the reduction of S. The frequency of the dominant resonant mode (mode 2) for $S = 500$ nm is very close to that of the unpatterned thin film, but with the decrease in S, the position of this peak shifts slightly toward lower frequency. This is due to the relative increase in the demagnetized regions between the antidots, which produces lower effective fields in these regions as opposed to the unpatterned thin film as shown later in this article. The higher frequency peak (mode 1), on the other hand, shifts to even higher frequency with the decrease in S, and the band gap opens up further. At $S = 200$ nm, a drastic change occurs in the frequency spectra and four clear bands of modes appear in the frequency range between 3 and 26 GHz.

We have performed micromagnetic simulations using the OOMMF software[28] by considering finite arrays of 7 × 7 antidots with varying lattice constants. Figure 2c shows the FFT spectra of the simulated time-domain magnetizations for all four samples. The simulations qualitatively reproduce the observed features, although the precise values of the frequencies and relative intensities are not always reproduced. This is expected due to the deviation of the simulated samples and conditions from the experimental samples and conditions. In general, the deviation in the dimensions as observed in the experimental samples are included in the simulated samples, but the precise edge roughness profiles are not possible to include in the finite difference method based micromagnetic simulations used here, where samples are divided into rectangular prism-like cells. The simulated arrays are much smaller (7 × 7 antidots) than the experimental samples (up to 50 × 50 antidots) due to the limitation in the computational resources. Possible changes in the magnetic parameters in the Ga⁺ implanted regions
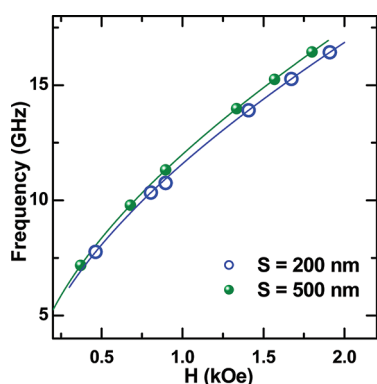
Figure 3. Experimental precession frequencies (symbols) and the fit to Kittel's formula (solid curve) for two antidot lattices with S = 200 and 500 nm.
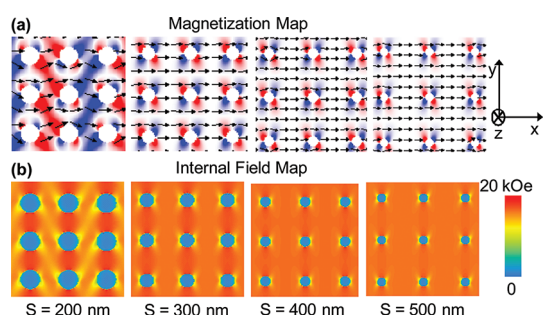

Figure 4. Projection on the $x-y$ plane of the spatial maps of (a) magnetization and (b) internal field for the Co antidot lattices with lattice constants S = 200, 300, 400, and 500 nm. The y-component of magnetization is represented by blue-white-red colormaps, while the colormap for the internal field is shown next to (b).

Figure 5. Simulated power (A) and phase (P) maps of different resonant modes for the antidot lattices with lattice constants S = 500, 400, 300, and 200 nm. The colormaps for the power and phase distributions are shown at the top of the figure.

could not be characterized and included in the simulation. Finally, the optical excitation in the experimental sample is simulated as an effective pulsed magnetic field-induced excitation. Despite all of these deviations, we observe the increase in the band gap between two frequency bands as S varies from 500 to 300 nm and occurrence of four frequency bands for S = 200 nm from the simulation.

Figure 3 shows the bias field dependence of the resonant mode at around 11 GHz in the magnonic spectra for the antidot lattices with S = 200 and 500 nm. The mode frequencies for the lattice with S = 200 nm are slightly down-shifted from those for the lattice with S = 500 nm. The solid curves show the fit with the Kittel's formula, and the extracted effective magnetization for the two different lattices are 1310 and 1380 emu/cc, respectively. This is confirmed by the simulated spatial distribution of magnetization (Figure 4a), which shows that the fraction of the demagnetized volume increases with the decrease in the lattice constant. The average magnetization values calculated from Figure 4a are identical to the values obtained from the fit to the Kittel's formula. In Figure 4b, we show the simulated internal field maps, which resemble the magnetization maps and would play key roles
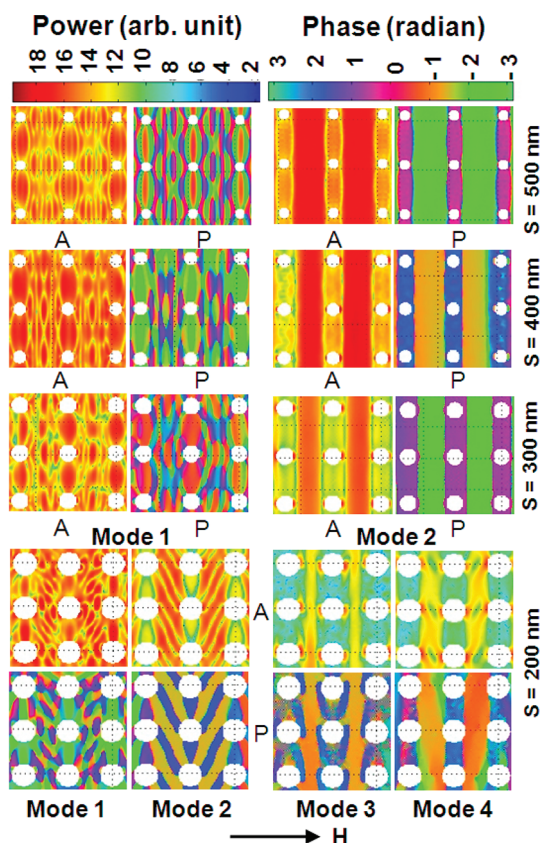
in the spatial profiles of the resonant modes, as described below.

Micromagnetic Simulations of Resonant Mode Profiles. In order to understand the mode profiles corresponding to each resonant peak, we have calculated the power and phase maps of the resonant modes by using a home-built code.[29] Due to the finite size of the array, the boundaries of the arrays experience non-uniform magnetostatic environment and consequently show boundary effect. Hence, we concentrate on 3 × 3 antidots from the center of the simulated lattices, for which the magnetostatic environment is almost identical. Figure 5 shows the power and phase maps for the main resonant peaks for antidot lattices with S = 500, 400, 300, and 200 nm. The bias field is applied parallel to the horizontal edges of the samples. The high frequency mode (mode 1) for 500 nm $\leq S \leq$ 300 nm corresponds to quantized spin wave modes with quantization axis parallel to the bias field. On the other hand, the low frequency mode (mode 2) corresponds to extended spin wave mode with wavevector perpendicular to the applied bias field, that is, in the magnetostatic surface wave (MSSW) mode geometry. The frequency of this mode is slightly reduced compared to the unpatterned thin films because of the
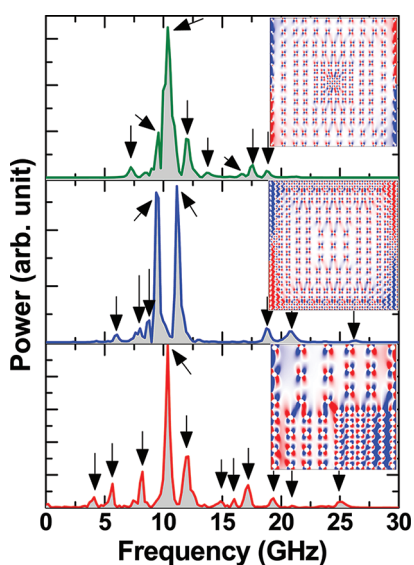
Figure 6. Simulated magnonic spectra of composite antidot structures consisting of arrays of square lattices with variable lattice constants arranged in three different geometries. The simulated static magnetization configurations of the composite structures are shown in the inset. The arrows indicate various peaks observed in the magnonic spectra.

modulation by the antidot structures and the ensuing demagnetized regions around the antidots. With the decrease in the lattice parameter, the quantization number of the spin wave modes for mode 1 is reduced, while mode 2 remains identical with a slight reduction in the amplitude down to $S = 300$ nm. However, a drastic change occurs at $S = 200$ nm. For $S = 200$ nm, mode 1 and mode 2 are quantized modes with their quantization axes parallel to the diagonal of the antidot lattice (rotated by 45° from those observed in 500 nm $\leq S \leq$ 300 nm). Mode 3 is identified as the MSSW mode with much reduced intensity, while mode 4 has a modulated MSSW-like profile.

Magnonic Spectra of Composite Antidot Structures. The tunability of magnonic spectra including the magnonic band gap can be applied to design nanoscale microwave filters in the form of a composite antidot structure formed of variable lattice constants. In order to demonstrate that we have considered three different composite antidot structures with variable lattice constants arranged in a checkerboard pattern, the patterns consist of radially increasing and decreasing lattice constants. Figure 6 shows the numerically calculated magnonic spectra for three different

composite structures along with their static magnetic configurations in the inset. In all three structures, rich magnonic spectra are observed. However, the bandwidth is maximum (27 GHz) for the structure shown in the middle panel, while the numbers of bands vary with the geometry of the structure (11 bands for the checkerboard pattern and 8 bands each for the other two structures). The observed spectra clearly go beyond the linear superposition of the bands observed for the constituent lattices. More importantly, the arrangement of the constituent lattices in the composite structure plays an important role in determining the magnonic spectra both qualitatively and quantitatively. This is because of the geometry-dependent creation of additional demagnetization regions in the composite structures, which is more prominent in the checkerboard pattern due to the sudden variation in the lattice constants at the joining regions and less prominent in the other two structures due to the continuous variation in the lattice constants in the structures. This is also evident in the static magnetic configurations of the three structures. The dependence of magnonic spectra on the arrangements of the constituent lattices in the composite structures provides an additional control parameter in the design of magnonic devices based upon composite antidot structures.

CONCLUSIONS

In summary, we have fabricated high-quality Co antidot lattice structures by using focused ion beam lithography. We have excited and detected the magnetization dynamics in those antidot lattice structures by an all-optical time-resolved Kerr microscope. The dynamics shows two prominent magnonic bands for sparsely packed lattices with a clear band gap. The band gap increases with the decrease in the lattice constant, and at the lowest value of the lattice constant, four distinct magnonic bands appear. The observations are qualitatively reproduced by micromagnetic simulations, and the mode profiles of the resonant modes are calculated and interpreted. We further demonstrate the tunability of magnonic spectra in composite antidot structures with varying geometry. The observations are important for potential applications of the antidot lattices in nanoscale magnonic crystals in the form of composite antidot structures with tunable band gap.

METHODS

Fabrication. Square arrays of Co antidots were prepared on 10×10 μm^2 blanket Co films by focused ion beam lithography. Arrays of 10×10 μm^2 resist patterns were first prepared on a Si/SiO$_2$ substrate by UV photolithography. The Co film was deposited onto the resist pattern by e-beam evaporation at a base pressure of about 2×10^{-8} Torr. A 10 nm thick SiO$_2$ capping layer was deposited on top of the Co film to protect the sample

from degradation when exposed to the optical pump−probe experiments in air. This is followed by the lifting off of the sacrificial material to obtain the blanket Co films. In the next step, the antidot arrays are fabricated on the blanket Co films by using focused liquid Ga$^+$ ion beam lithography (Helios NANO-LAB 600, dual beam FIB). The optimal parameters for milling were found to be 30 kV voltage and 28 pA current. In FIB, the spot size used for milling needs to be optimized not only for

creating repetitive nanopatterns with high fidelity but also to ensure that the material that has been retained after patterning (Co films in this case) does not have excessive Ga$^+$ ion implantations. The spot size is a function of the beam current. We have used a beam current of 28 pA that gives sufficient etch rate yet limits the spot size to around 8 nm. The thickness of the Co film (25 nm) is smaller than the stopping range of Ga$^+$ ions at 30 keV, which ensures that the ions stop within the SiO_2 layer underneath the film. There are two types of damage that can occur on the Co film during the milling process. One is the direct damage that affects the edges of the holes due to direct beam of finite width. The other is the struggling of the ion beam that causes lateral implantation in the bulk of the film along the edges. The presence of a 10 nm thick SiO_2 capping layer protects the unmilled Co film to a large extent from direct irradiation. However, there will be some finite damages at the edges of the antidots due to Ga$^+$ ion implantation occurring laterally. Simulations of ion trajectory and damage profile on Co(25 nm)/ SiO_2 (10 nm) film using the experimental parameters show that the lateral damages are located within about 5 nm from the edges. This is much less than the antidot separation (S), thus ensuring that predominant magnetization precession occurs in regions that do not have appreciable defects. The initial preparation of the 100 nm holes was done by focused ion beam milling at 30 kV voltage in single pass. The redepositions that occurred during the initial milling were then removed by a final milling at 2 kV voltage in multipass mode (200 passes), which makes the holes much cleaner with uniform edges.

Measurement. The ultrafast magnetization dynamics was measured by using a home-built time-resolved magneto-optical Kerr effect microscope based upon a two-color collinear pump–probe setup. The second harmonic ($\lambda = 400$ nm, pulse width ~100 fs, average power = 10 mW) of a Ti:sapphire laser (Tsunami, Spectra Physics, pulse width ~70 fs) was used to pump the samples, while the time-delayed fundamental ($\lambda = 800$ nm, average power = 2.5 mW) laser beam was used to probe the dynamics by measuring the polar Kerr rotation by means of a balanced photodiode detector. The probe beam is focused to a spot size of 800 nm and placed at the center of each lattice by a microscope objective with numerical aperture NA = 0.65. The pump beam is spatially overlapped with the probe beam after passing through the same microscope in a collinear geometry. A large magnetic field is first applied at a small angle (~15°) to the sample plane to saturate its magnetization. The magnetic field strength is then reduced to the bias field value (H = component of bias field along the x-direction), which ensures that the magnetization remains saturated along the bias field direction. The pump beam was chopped at 2 kHz frequency, and phase-sensitive detections of the Kerr rotation and reflectivity were used.

Numerical Simulation. The static magnetic configuration at the applied bias field was obtained by first applying a large magnetic field to saturate the sample and then by reducing the field to bias field value and allowing the system to reach the equilibrium (maximum torque $m \times H$, where $m = M/M_S$ goes well below 10^{-6} A/m). The dynamics was obtained by applying a pulsed magnetic field and by calculating the spatial distribution of magnetization at time steps of 5 ps for a total duration of 4 ns. The convergence criterion for the dynamical calculation is set on the time steps. The spatial profile of the power and phase information for various resonant modes are obtained by fixing one of the spatial coordinates in the space and time-dependent magnetization and then by performing a discrete Fourier transform with respect to time domain.

Conflict of Interest: The authors declare no competing financial interest.

REFERENCES AND NOTES

1. Kern, K.; Heitmann, D.; Grambow, P.; Zhang, Y. H.; Ploog, K. Collective Excitations in Antidots. *Phys. Rev. Lett.* **1991**, *66*, 1618–1621.
2. Diwekar, M.; Kamaev, V.; Shi, J.; Vardeny, Z. V. Optical and Magneto-Optical Studies of Two-Dimensional Metallodielectric Photonic Crystals on Cobalt Films. *Appl. Phys. Lett.* **2004**, *84*, 3112–3114.
3. Ctistis, G.; Papaioannou, E.; Patoka, P.; Gutek, J.; Fumagalli, P.; Giersig, M. Optical and Magnetic Properties of Hexagonal Arrays of Subwavelength Holes in Optically Thin Cobalt Films. *Nano Lett.* **2009**, *9*, 1–6.
4. Torres, L.; Lopez-Diaz, L.; Alejos, O. Micromagnetic Analysis of Recording Processes in Periodic Antidot Arrays: Interaction between Adjacent Bits. *J. Appl. Phys.* **2000**, *87*, 5645–5647.
5. Wang, C. C.; Adeyeye, A. O.; Singh, N. Magnetic Antidot Nanostructures: Effect of Lattice Geometry. *Nanotechnology* **2006**, *17*, 1629–1636.
6. Neusser, S.; Grundler, D. Magnonics: Spin Waves on the Nanoscale. *Adv. Mater.* **2009**, *21*, 2927–2932.
7. Kruglyak, V. V.; Demokritov, S. O.; Grundler, D. Magnonics. *J. Phys. D: Appl. Phys.* **2010**, *43*, 264001.
8. Chumak, A. V.; Tiberkevich, V. S.; Karenowska, A. D.; Serga, A. A.; Gregg, J. F.; Slavin, A. N.; Hillebrands, B. All-Linear Time Reversal by a Dynamic Artificial Crystal. *Nat. Commun.* **2010**, *1*, 141.
9. Ma, F. S.; Lim, H. S.; Wang, Z. K.; Piramanayagam, S. N.; Ng, S. C.; Kuok, M. H. Micromagnetic Study of Spin Wave Propagation in Bicomponent Magnonic Crystal Waveguides. *Appl. Phys. Lett.* **2011**, *98*, 153107.
10. Duerr, G.; Madami, M.; Neusser, S.; Tacchi, S.; Gubbiotti, G.; Carlotti, G.; Grundler, D. Spatial Control of Spin-Wave Modes in $Ni_{80}Fe_{20}$ Antidot Lattices by Embedded Co Nanodisks. *Appl. Phys. Lett.* **2011**, *99*, 202502.
11. Yu, M.; Malkinski, L.; Spinu, L.; Zhou, W.; Whittenburg, S. Size Dependence of Static and Dynamic Magnetic Properties in Nanoscale Square Permalloy Antidot Arrays. *J. Appl. Phys.* **2007**, *101*, 09F501.
12. Yu, C. T.; Jiang, H.; Shen, L.; Flanders, P. J.; Mankey, G. J. The Magnetic Anisotropy and Domain Structure of Permalloy Antidot Arrays. *J. Appl. Phys.* **2000**, *87*, 6322–6324.
13. Toporov, A. Y.; Langford, R. M.; Petford-Long, A. K. Lorentz Transmission Electron Microscopy of Focused Ion Beam Patterned Magnetic Antidot Arrays. *Appl. Phys. Lett.* **2000**, *77*, 3063–3065.
14. Tacchi, S.; Madami, M.; Gubbiotti, G.; Carlotti, G.; Adeyeye, A. O.; Neusser, S.; Botters, B.; Grundler, D. Magnetic Normal Modes in Squared Antidot Array with Circular Holes: A Combined Brillouin Light Scattering and Broadband Ferromagnetic Resonance Study. *IEEE Trans. Magn.* **2010**, *46*, 172–178.
15. Tacchi, S.; Madami, M.; Gubbiotti, G.; Carlotti, G.; Adeyeye, A. O.; Neusser, S.; Botters, B.; Grundler, D. Angular Dependence of Magnetic Normal Modes in NiFe Antidot Lattices with Different Lattice Symmetry. *IEEE Trans. Magn.* **2010**, *46*, 1440–1443.
16. Neusser, S.; Duerr, G.; Tacchi, S.; Madami, M.; Sokolovskyy, M. L.; Gubbiotti, G.; Krawczyk, M.; Grundler, D. Magnonic Minibands in Antidot Lattices with Large Spin-Wave Propagation Velocities. *Phys. Rev. B* **2011**, *84*, 094454.
17. Neusser, S.; Duerr, G.; Bauer, H. G.; Tacchi, S.; Madami, M.; Woltersdorf, G.; Gubbiotti, G.; Back, C. H.; Grundler, D. Anisotropic Propagation and Damping of Spin Waves in a Nanopatterned Antidot Lattice. *Phys. Rev. Lett.* **2010**, *105*, 067208.
18. Neusser, S.; Botters, B.; Becherer, M.; Schmitt-Landsiedel, D.; Grundler, D. Spin-Wave Localization between Nearest and Next-Nearest Neighboring Holes in an Antidot Lattice. *Appl. Phys. Lett.* **2008**, *93*, 122501.
19. McPhail, S.; Gürtler, C. M.; Shilton, J. M.; Curson, N. J.; Bland, J. A. C. Coupling of Spin-Wave Modes in Extended Ferromagnetic Thin Tilm Antidot Arrays. *Phys. Rev. B* **2005**, *72*, 094414.
20. Martyanov, O. N.; Yudanov, V. F.; Lee, R. N.; Nepijko, S. A.; Elmers, H. J.; Hertel, R.; Schneider, C. M.; Schönhense, G.

Ferromagnetic Resonance Study of Thin Film Antidot Arrays: Experiment and Micromagnetic Simulations. *Phys. Rev. B* **2007**, *75*, 174429.

21. Kostylev, M.; Gubbiotti, G.; Carlotti, G.; Socino, G.; Tacchi, S.; Wang, C.; Singh, N.; Adeyeye, A. O.; Stamps, R. L. Propagating Volume and Localized Spin Wave Modes on a Lattice of Circular Magnetic Antidots. *J. Appl. Phys.* **2008**, *103*, 07C507.

22. Grimes, C. A.; Trouilloud, P. L.; Lumpp, J. K.; Bush, G. C. Permeability Spectra of Hole Arrays Defined on Single Layer Permalloy Thin Films. *J. Appl. Phys.* **1997**, *81*, 4720–4722.

23. Ding, J.; Tripathy, D.; Adeyeye, A. O. Effect of Antidot Diameter on the Dynamic Response of Nanoscale Antidot Arrays. *J. Appl. Phys.* **2011**, *109*, 07D304.

24. Ulrichs, H.; Lenk, B.; Münzenberg, M. Magnonic Spin-Wave Modes in CoFeB Antidot Lattices. *Appl. Phys. Lett.* **2010**, *97*, 092506.

25. Neusser, S.; Botters, B.; Grundler, D. Localization, Confinement, and Field-Controlled Propagation of Spin Waves in $Ni_{80}Fe_{20}$ Antidot Lattices. *Phys. Rev. B* **2008**, *78*, 054406.

26. Barman, A. Control of Magnonic Spectra in Cobalt Nanohole Arrays: the Effects of Density, Symmetry and Defects. *J. Phys. D: Appl. Phys.* **2010**, *43*, 195002.

27. Rana, B.; Kumar, D.; Barman, S.; Pal, S.; Fukuma, Y.; Otani, Y.; Barman, A. Detection of Picosecond Magnetization Dynamics of 50 nm Magnetic Dots down to the Single Dot Regime. *ACS Nano* **2011**, *5*, 9559–9565.

28. Donahue, M.; Porter, D. G. OOMMF User's guide, version 1.0, Interagency Report NISTIR 6376, National Institute of Standard and Technology, Gaithersburg, MD, 1999; http://math.nist.gov/oommf.

29. Kumar, D.; Dmytriiev, O.; Ponraj, S.; Barman, A. Numerical Calculation of Spin Wave Dispersions in Magnetic Nanostructures. *J. Phys. D: Appl. Phys.* **2012**, *45*, 015001.